JACS Au
AN OPEN ACCESS JOURNAL OF THE AMERICAN CHEMICAL SOCIETY

pubs.acs.org/jacsau

Article

A Preinstalled Protic Cation as a Switch for Superprotonic Conduction in a Metal–Organic Framework

Kazuya Otsubo,* Shuya Nagayama, Shogo Kawaguchi, Kunihisa Sugimoto, and Hiroshi Kitagawa*

Cite This: *JACS Au* 2022, 2, 109–115

Read Online

ACCESS | Metrics & More | Article Recommendations | Supporting Information

ABSTRACT: Metal–organic frameworks (MOFs), made from various metal nodes and organic linkers, provide diverse research platforms for proton conduction. Here, we report on the superprotonic conduction of a Pt dimer based MOF, $[Pt_2(MPC)_4Cl_2Co(DMA)(HDMA)\cdot guest]$ (H_2MPC, 6-mercaptopyridine-3-carboxylic acid; DMA, dimethylamine). In this framework, a protic dimethylammonium cation ($HDMA^+$) is trapped inside a pore through hydrogen bonding with an MPC ligand. Proton conductivity and X-ray measurements revealed that trapped $HDMA^+$ works as a preinstalled switch, where $HDMA^+$ changes its relative position and forms an effective proton-conducting pathway upon hydration, resulting in more than 10^5 times higher proton conductivity in comparison to that of the dehydrated form. Moreover, the anisotropy of single-crystal proton conductivity reveals the proton-conducting direction within the crystal. The present results offer insights into functional materials having a strong coupling of molecular dynamic motion and transport properties.

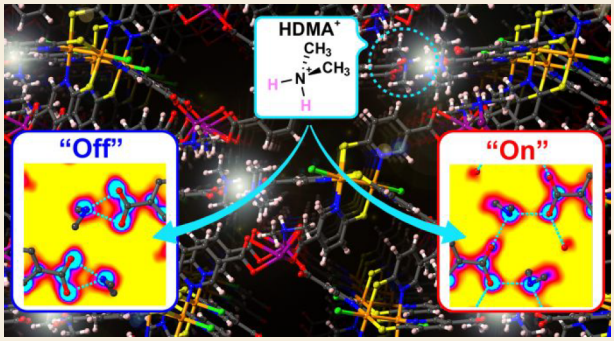

KEYWORDS: *metal–organic frameworks, polynuclear-metal complexes, platinum, proton conduction, structural transition*

INTRODUCTION

Metal–organic frameworks (MOFs), which are crystalline polymeric microporous materials made from metal ions linked to organic ligands, have applications in a wide variety of fields, such as gas storage and separation, catalysis, and switching properties.[1−5] In comparison with other classical porous materials such as activated carbon[6,7] and zeolites,[8,9] MOFs have high degrees of freedom of the polynuclear metal node and multidentate organic ligand selection. Accordingly, MOFs enable diversity in structural design, tunable surface area, porosity, and physical properties.[10−14] Among them, MOFs have recently been intensely studied as a versatile platform for proton conductors toward their potential application as solid-state electrolytes of fuel cells. Due to the structural designability, a large number of proton-conductive MOFs have been developed and thoroughly studied.[15−19] The design strategy of highly proton conductive MOFs is classified into the following three types: type I incorporates protic ions (i.e., H_3O^+ and NH_4^+) into the pore, type II attaches acidic functional groups (i.e., −COOH, $-SO_3H$, and $-PO_3H_2$) on the pore, and type III includes guests (i.e., imidazole and adipic acid) as a proton source.[20,21] The proton-conducting mechanism can be classified into two mechanisms: one is the Grotthuss mechanism,[22,23] where the protons diffuse through hydrogen bonds between the conducting media such as H_3O^+–H_2O, and the other is the vehicle mechanism,[24] which is a direct diffusion of mobile carriers (i.e., H_3O^+).

Among the polynuclear metal units, Pt dimer complexes are known not only as building blocks for electrically conductive one-dimensional (1D) coordination polymers but also as key units for unique optical properties in the solid state due to metal–metal interactions.[25−29] Many kinds of polynuclear metal complexes have been used for secondary building units (SBUs) of MOFs,[10−12] but only a few series of 1D coordination polymers based on a Pt dimer have been achieved.[30−34] Notably, there has been no report on Pt dimer based MOFs with 2D and 3D extended structures. In this work, we have designed a novel MOF based on a Pt dimer complex, $Pt_2(HMPC)_4$ (H_2MPC, 6-mercaptopyridine-3-carboxylic acid) shown in Figure 1a. This platinum dimer unit has four additional carboxyl groups, which can be expected to act as coordination sites for other metal ions.[35] We successfully obtained a novel MOF, $[Pt_2(MPC)_4Cl_2Co(DMA)(HDMA)\cdot guest]_n$ (**1**; DMA, dimethylamine), from a solvothermal reaction using $Pt_2(HMPC)_4$ and cobalt ion. To the best of our knowledge, **1** is the first example of a MOF based on a platinum dimer SBU. In the solid state, the dimethylammo-

Received: September 3, 2021
Published: January 3, 2022

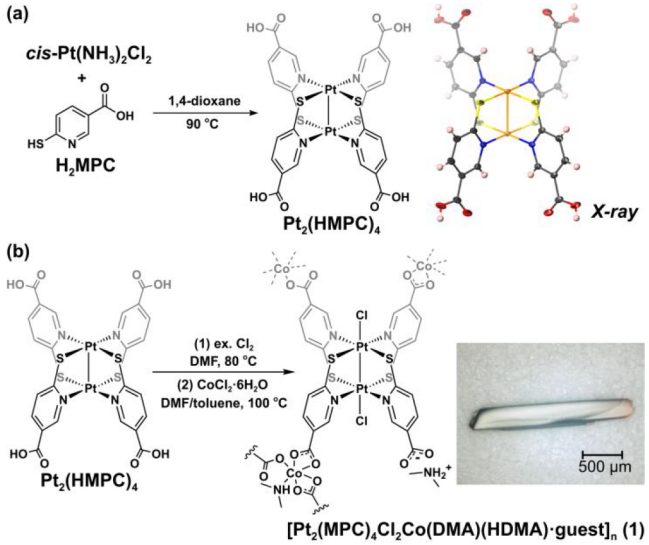

Figure 1. Schematic representation of the synthetic route of the Pt dimer based MOF **1**: (a) synthetic scheme and X-ray molecular structure of the divalent Pt dimer unit, $Pt_2(HMPC)_4$; (b) solvothermal synthesis of **1**. A typical example of a single crystal is shown on the right.

nium cation, $HDMA^+$, is trapped by a carboxylate group of the organic ligand part. We found that the trapped protic $HDMA^+$ cation works as a preinstalled switch with a change in relative position to make an effective proton-conducting pathway upon hydration, as evidenced by a proton conductivity that was more than 10^5 times higher than that of the activated form and by synchrotron powder X-ray structural analyses. Although the measurement of single-crystal conductivity is a crucial technique to confirm the conducting pathway, the proton conductivity of MOFs measured along multiple crystallographic axes has rarely been discussed.[36,37] This time, on the basis of the anisotropy of single-crystal proton conductivity, the proton-conducting direction is also successfully demonstrated.

RESULTS AND DISCUSSION

Synthesis and Structural Characterization

The synthetic route for the new MOF **1** is shown in Figure 1. First, the divalent Pt dimer $Pt_2(HMPC)_4$ was obtained from the reaction of cisplatin and the ligand H_2MPC (Figure 1a) according to a method similar to that in a previous report.[38] We also confirmed the molecular structure by single-crystal X-ray crystallography. Next, using the $Pt_2(HMPC)_4$ as the starting material, **1** was obtained as needle-shaped single crystals from an oxidation reaction using Cl_2 gas followed by a solvothermal reaction with Co ion (Figure 1b). From the results of elemental analyses, including Cl and S analyses, **1** contains coordinated and noncoordinated guests (see the Supporting Information for details).

We investigated the crystal structure of **1** by single-crystal X-ray crystallography (Figure 2 and Figures S1–S6). It is clear that **1** is composed of a Pt dimer unit and a Co ion (Figure 2a,b). Focusing on each metal center, we can see that the Pt part has a clear paddlewheel-type dimer structure, where an MPC ligand coordinates with two Pt ions as an in-plane ligand and two chloride ions coordinate to the apical position of each Pt ion (Figure S1). This indicates that the Pt ion is trivalent, as seen in many previous examples.[27,30] The existence of a Pt dimer unit is also reflected in the characteristic vibration modes and the electronic transition and supported by a density functional theory (DFT) calculation (Figures S7–S9 and Tables S1 and S2). Three out of the four carboxyl groups of the MPC ligand in the Pt dimer and the neutral DMA coordinate with a trivalent Co ion, forming a six-coordinated octahedral geometry (Figure S2). The valence states of Pt and Co ions were also confirmed by X-ray photoelectron spectroscopy (Figure S10). Without the noncoordinated DMA and H_2O, the structure contains a large void (31% of the unit cell volume, calculated by PLATON;[39] see also Figure S3). From the solvent-accessible surface map (Figure 2c and Figure S4), two kinds of channels along the $a-c$ direction (channel A) and the b direction (channel B) were found, and they were linked. The isolated cavity C was also formed. The overall structure (Figure 2b) is composed of a stacked 2D layer structure along the $a-c$ direction (Figure S5). The adjacent 2D layers are linked through two kinds of intermolecular interactions, namely a short S–S contact (~3.38 Å, Figure S6) and a ligand–guest hydrogen bond (Figure 2d). In the structure, one of the four carboxyl groups ($-COO^-$) of the MPC ligand in the Pt dimer interacts with guest DMA via hydrogen bonding, making an acid–base pair. The difference Fourier map indicated that the guest DMA was protonated (H6A and H6B) to form $HDMA^+$, where one $HDMA^+$ was shared by two carboxyl groups (Figure S11). As a result, a 1D hydrogen-bonding network was formed along the b axis. Because this kind of protic $HDMA^+$ works as a good proton source of a proton-conductive MOF,[37,40−43] **1** was expected to display high proton conduction.

Proton Conductivity

Because noncoordinated DMA and H_2O can be easily removed above room temperature (RT), as confirmed by thermogravimetric analysis (Figure S12), the H_2O sorption isotherm was measured on an activated form of **1** at 25 °C. A high uptake of H_2O was observed, and the total amount of adsorbed H_2O was about 16 molecules per formula unit (Figure 3a). A sharp increase in adsorbed amount was observed at $P/P_0 \approx 0.8$, suggesting the formation of continuous hydrogen-bonding networks among the guest molecules inside the pore. As discussed above, the obtained **1** had a protic $HDMA^+$ guest, forming a hydrogen-bonding network categorized as type I or III in highly proton-conductive MOFs.[20,21] Therefore, alternate current (AC) impedance spectroscopy measurements on pelletized polycrystalline powder were examined (Figure 3 and Figures S13 and S14). Prior to AC impedance measurements, the powder sample was evacuated at RT to remove noncoordinated guests, same as the H_2O sorption measurement condition.

Figure 3a shows the relative humidity (RH) dependence of the proton conductivity at 25 °C. The proton conductivity significantly increased with increasing RH, reaching 1.4×10^{-3} S cm^{-1} at 95% RH and 25 °C. It is worth noting that a conductivity jump was observed at 80% RH, where a sharp increase in H_2O sorption occurs. As is clearly observed, at 60 °C (95% RH), the proton conductivity reached 7.1×10^{-3} S cm^{-1} in the range of superprotonic conductivity (Figure 3b and Figure S13d). From the Arrhenius plots, the activation energy was estimated to be 0.40 eV, suggesting that the proton-conducting mechanism is expected to be similar to the Grotthuss mechanism (Figure 3b).[22,23,44] For comparison, the

https://doi.org/10.1021/jacsau.1c00388
JACS Au 2022, 2, 109–115

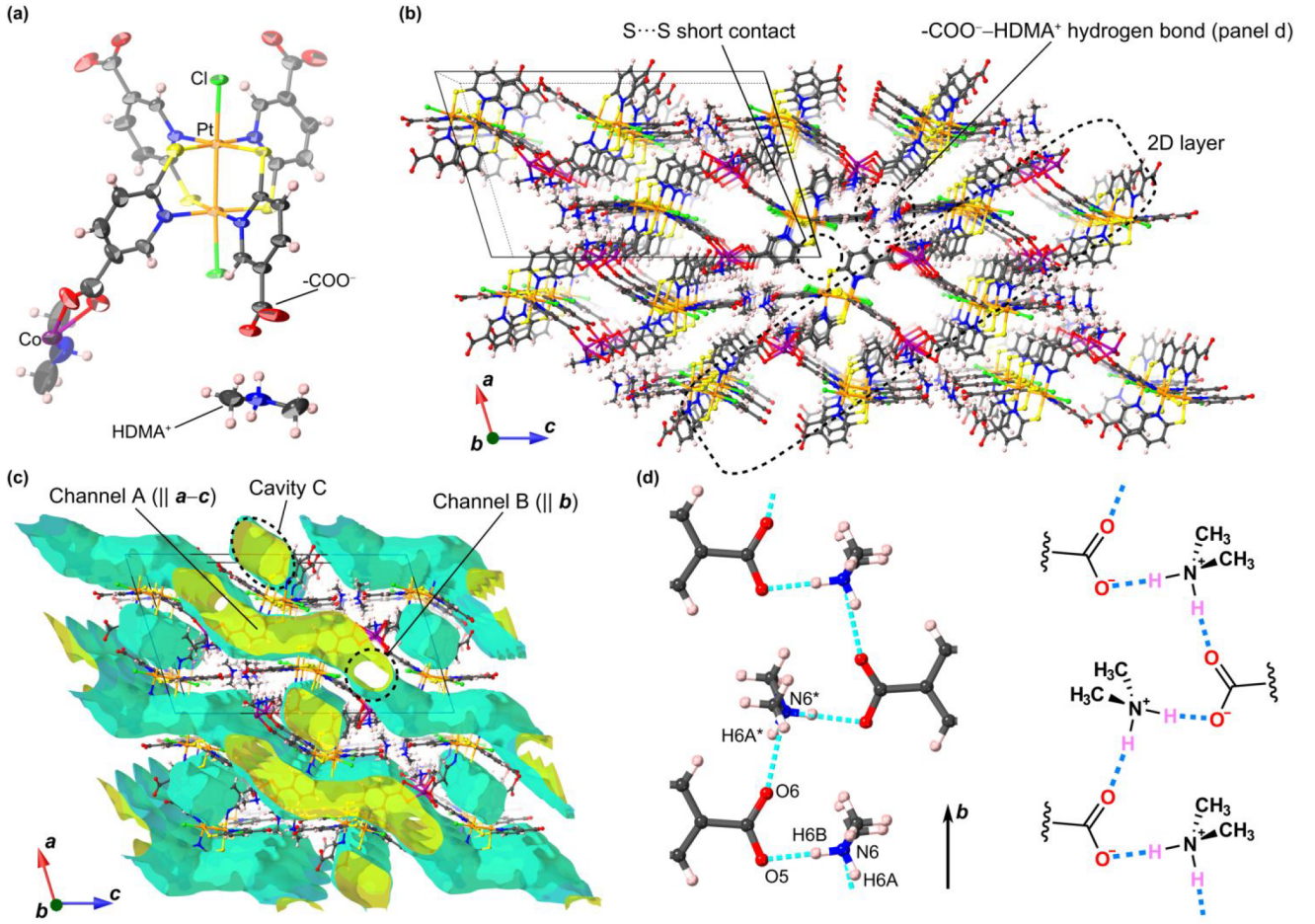

Figure 2. X-ray crystal structure of **1** at 100 K. (a) ORTEP drawing of the asymmetric unit (50% probability). (b) 3D packing structure along the *b* axis. Representative structural component and intermolecular interactions are denoted as dotted lines. (c) Solvent-excluded surface representation in the packing structure (probe radius: 1.4 Å). (d) X-ray structure (left) and schematic representation (right) of the carboxyl groups ($-COO^-$) of the MPC ligand–guest $HDMA^+$ pairs. The N6···O5 and N6···O6 distances are 2.72 and 2.80 Å (light blue dotted lines), respectively. Pt, Co, Cl, S, C, N, O, and H atoms are shown in orange, purple, green, yellow, gray, blue, red, and pink, respectively. For (a)–(c), the structures are drawn in a ball-and-stick model, and noncoordinated DMA and H_2O molecules are omitted.

proton conductivity under anhydrous conditions was examined (0% RH, Figure 3b and Figure S13e). Although protic $HDMA^+$ was present in the structure, the observed proton conductivity was more than 5 orders of magnitude lower than that under the hydrous condition. These results indicate that both the $HDMA^+$ cation and adsorbed H_2O contribute to the superprotonic conduction, where protic $HDMA^+$ works as an effective proton source and protons can migrate through the continuous hydrogen-bonding networks among carboxyl groups of MPC, $HDMA^+$, and adsorbed H_2O.

The anisotropy of proton conductivity was also investigated using the single-crystal sample to clarify the proton-conducting pathway (Figure 3a and Figures S15–S17). For the single-crystal AC impedance measurement, gold electrodes and wires were attached along specific crystallographic axes: the [100], [010], and [001] directions (Figure S15). A high proton conductivity above 10^{-4} S cm^{-1} was observed in each experimental direction (Figure 3a). At 95% RH and 25 °C, the highest proton conductivity of 1.6×10^{-3} S cm^{-1} was observed along the [010] direction (i.e., ∥ to the *b* axis), whereas lower conductivities of 2.7×10^{-4} and 1.8×10^{-4} S cm^{-1} were observed along the [100] and [001] directions, respectively. It should be noted that the proton conductivity along the [010] direction reached 2.2×10^{-2} S cm^{-1} at 95% RH and 60 °C, higher by a factor of 20 than that in the [001] direction (Figures S16 and S17). The observed proton conductivity is very high and is among the most proton conductive MOFs reported to date, which is comparable to that of the practical proton-exchange polymer Nafion used in fuel cells.[17−19,21] In addition, the overlapping peaks in the impedance and modulus spectra indicate the long-range migration of protons (Figure S16d).[45] The conductivity along the [010] direction was in the same range as that of the pelletized sample, suggesting that an effective proton-conducting pathway is formed along the *b* axis.

Humidity-Dependent Movement of the Proton Source

To clarify in detail in the origin of realization of the superprotonic conduction, the crystal structures of activated (**1A**) and hydrated (**1H**) forms were analyzed. Because **1** loses single crystallinity upon the activation and hydration processes, we analyzed both structures using a Rietveld refinement on synchrotron powder X-ray diffraction data (Figure S18). Using the single-crystal X-ray structure of **1** as an initial structure, both structures were successfully determined with good reliability factors (Figures S19–S22). Both **1A** and **1H** have structures similar to that of the original as-synthesized **1**, but there is a clear difference in the hydrogen bonds between MPC

https://doi.org/10.1021/jacsau.1c00388
JACS Au 2022, 2, 109–115

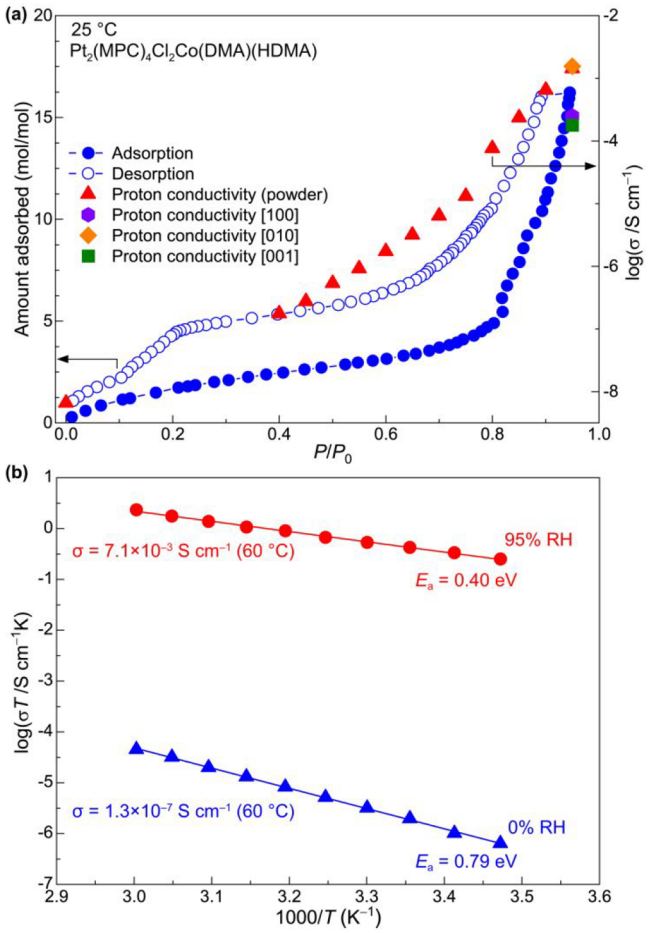

Figure 3. Sorption and proton-conducting properties of **1**. (a) Water vapor adsorption/desorption isotherms (circles) and humidity dependence of proton conductivity (triangles) at 25 °C. (b) Arrhenius plots of the proton conductivity under 95% (circles) and 0% RH (triangles) conditions. Least-squares fitting results are also shown. In (a), conductivity values measured with a single-crystal sample (hexagon, diamond, and square) are also shown (see text).

and $HDMA^+$ (Figure 4). Figure 4a shows the relative positions of MPC and $HDMA^+$ (the same as in Figure 2d) on the basis of the Rietveld refinements. It is worth noting that the $HDMA^+$ changes its relative position along the *b* axis, suggesting a change in the hydrogen-bonding manner. To visualize the intermolecular interaction, the maximum-entropy method (MEM) was applied to the Rietveld refinement results (Figure 4b). Weak but clear charge densities (~0.7 e/Å^3) were found between MPC and $HDMA^+$ (white arrows), indicating a hydrogen bond.[46] Using these MEM charge density maps, different manners of hydrogen bonding were successfully visualized (Figure 4b,c). For **1H**, the 1D hydrogen-bonding network is almost the same as that of the as-synthesized **1**, where one $HDMA^+$ is shared by two carboxyl groups. In addition, there is an additional hydrogen bond between the carboxyl group and H_2O molecule (O5···O20; see also Figure 5b). In contrast, for **1A**, $HDMA^+$ changes its position and is strongly trapped by one carboxyl group, indicating that a 1D hydrogen-bonding network is not formed (Figure 4c).

Proton-Conducting Pathway

On the basis of the result of single-crystal AC impedance measurements and the structural differences between **1A** and

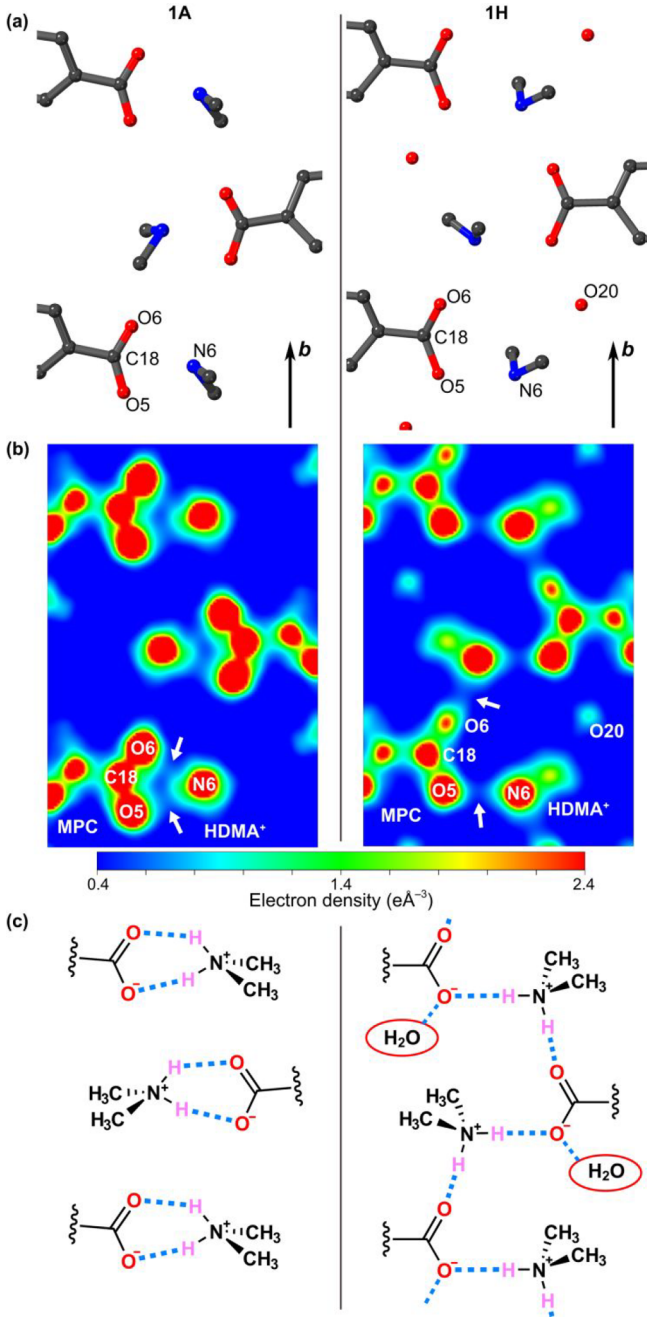

Figure 4. Difference in hydrogen bonds between MPC and $HDMA^+$ revealed by synchrotron powder X-ray analyses. X-ray structures (a), 2D MEM charge density views sliced in the (400) plane (b), and schematic representations of (c) **1A** (left) and **1H** (right). (a) and (c) are drawn as same as in Figure 2d. For (b), the 2D maps are drawn in the selected ranges ($-0.1 \le y \le 1.4$ and $0.1 \le z \le 0.4$) to fit (a) and (c). White arrows denote possible hydrogen bonds. For (a), the color code is same as in Figure 2.

1H, the realization of superprotonic conduction upon hydration can be explained as described in Figure 5: in **1A**, there is no hydrogen-bonding network, and protons cannot diffuse easily. Upon hydration, the protonated $HDMA^+$ slides like a preinstalled switch, where its relative position switches the hydrogen-bonding network from the "off" state (**1A**) to the "on" state (**1H**). The difference in the hydrogen-bonding energy of the MPC−$HDMA^+$ pair between the **1A** and **1H** states on the basis of the DFT calculations on simple model

https://doi.org/10.1021/jacsau.1c00388
JACS Au 2022, 2, 109−115

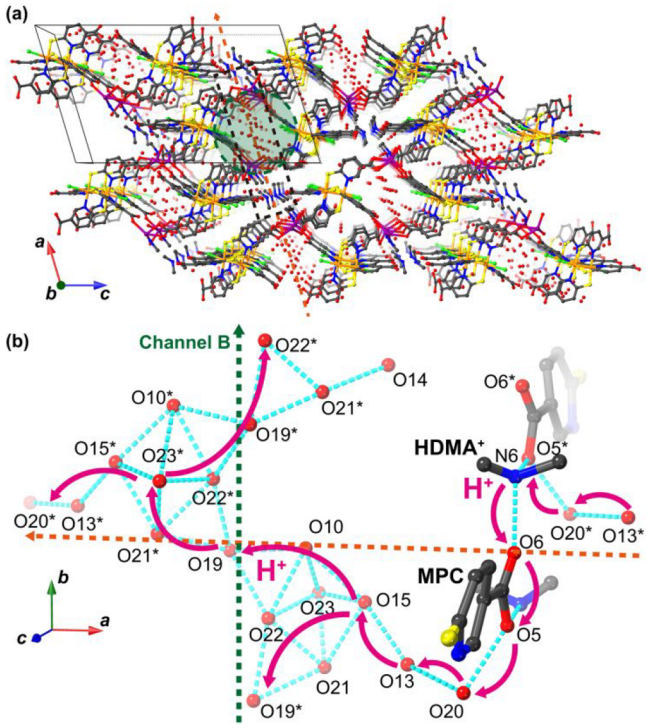

Figure 5. Plausible proton-conducting pathway in **1**. (a) 3D packing structure of **1H** along the *b* axis. (b) Schematic representation (depicted from the black dotted area in (a)) of the proton-conducting pathway of **1** based on the single-crystal proton conductivity measurements and a structural analysis. Isolated O atoms denote H_2O molecules of crystallization found in the structural analysis. Possible hydrogen bonds are drawn as light blue dotted bonds, where interatomic O···O and N···O distances are between 2.43 and 2.84 Å. The color code is the same as in Figure 2.

structures was estimated to be 0.33 eV, which is in good agreement with the difference in the activation energy (~0.4 eV) of proton conductivity (Figure S23 and Tables S3 and S4). The "on" state (**1H**) provides the 1D hydrogen-bonding network among the carboxyl groups of MPC, $HDMA^+$ cations, and adsorbed H_2O molecules along the *a* axis (see orange dotted line in Figure 5). Accordingly, a continuous hydrogen-bonding network among adsorbed H_2O molecules is formed simultaneously inside channel B (along the *b* axis; see green dotted line in Figure 5), where the protons provided from the $HDMA^+$ cation can diffuse easily within the crystal through this pathway; this is schematically shown by magenta arrows in Figure 5b (i.e., the Grotthuss mechanism). As was observed in Figure 3a, the significant increase in proton conductivity upon hydration is derived from the completion of continuous hydrogen-bonding networks among carboxyl groups, $HDMA^+$, and H_2O along the *a* and *b* axes. In addition, the fact that the highest single-crystal proton conductivity was observed along the *b* axis strongly supports the formation of an effective conducting pathway inside channel B.

CONCLUSION

In conclusion, we successfully synthesized the first example of a Pt dimer based MOF, **1**. In the crystal, protonated $HDMA^+$ is trapped as a guest through a hydrogen bond with the carboxyl group of the MPC ligand. The trapped $HDMA^+$ works as a preinstalled protic switch for superprotonic conduction, where its relative position changes from the "off" (activated) state to the "on" (hydrated) state upon water adsorption. The formation of the hydrogen-bonding network within the crystal is triggered by the humidity-dependent movement of the protic cation and plays an important role in an effective Grotthuss-type proton transport, as confirmed by an increase in proton conductivity by a factor of more than 10^5 upon hydration and also by synchrotron X-ray structural analyses. The anisotropy of proton conductivity based on the single-crystal conductivity measurements along multiple crystallographic axes was also discussed; it clearly indicated the direction of the effective proton-conducting pathway. The findings presented here will contribute to the further development of new switching materials with a molecular dynamic motion coupled proton transfer system.

EXPERIMENTAL SECTION

Synthesis of $[Pt_2(MPC)_4Cl_2Co(DMA)(HDMA)\cdot guest]_n$ (1)

A DMF solution of $Pt_2(HMPC)_4$ (20 mmol/L, 10 mL) was treated with Cl_2 and stirred at 80 °C for 12 h. To 3.5 mL of this solution were added a DMF solution of $CoCl_2\cdot 6H_2O$ (40 mmol/L, 0.5 mL) and toluene (0.5 mL), and the mixture was sealed in a screw-capped glass vial (15 mL). After heating at 100 °C for 72 h, single crystals were obtained by slow cooling (Yield: 55.6 mg, 62% based on $Pt_2(HMPC)_4$). Anal. (calcd, found) for $C_{28}H_{27}Cl_2CoN_6O_8Pt_2S_4\cdot DMA\cdot 0.5H_2O$: C (28.20, 28.33); H (2.76, 2.87); N (7.67, 7.44), Cl (5.55, 5.65); S (10.04, 10.05).

Single-Crystal X-ray Crystallography

An X-ray crystal structure analysis of **1** was carried out using a Bruker SMART APEX II CCD detector with graphite-monochromated Mo Kα radiation (λ = 0.71073 Å) at 100 K. A single crystal of **1** was mounted on MicroMesh (MiTeGen) with Paratone-N oil (Hampton Research) to avoid the loss of guest molecules. The details of the crystallographic data are described in the Supporting Information.

Sorption Experiment

Water vapor adsorption/desorption isotherms were measured using a BELSORP-max apparatus (MicrotracBEL Corp.). The polycrystalline powder sample (~100 mg) was dried under high vacuum (<10^{-1} Pa) at RT for 3 days prior to measurement.

Proton Conductivity

AC impedance measurements were carried out using a Solartron 1260 impedance/gain−phase analyzer and 1296 dielectric interface (frequency range: 10 MHz−1 Hz). The RH and temperature were controlled using an Espec Corp. SH-221 apparatus.

Powder X-ray Diffraction (PXRD)

Synchrotron PXRD data were measured in the range of 2θ = 1.5−50° with a step of 0.01° at 298 K, using a large Debye−Scherrer camera with imaging plate detector installed on the BL02B2 beamline at SPring-8, Japan. The incident X-rays were monochromated to 21.3 keV (λ = 0.58016 Å) with a Si (111) double-crystal monochromator. Polycrystalline powder samples in different states were sealed in a borosilicate glass capillary (WJM-Glas Müller GmbH). The details of the crystal structure determination are described in the Supporting Information.

ASSOCIATED CONTENT

Supporting Information

The Supporting Information is available free of charge at https://pubs.acs.org/doi/10.1021/jacsau.1c00388.

Full materials and methods, crystallographic data, supporting characterization data, and DFT calculations including additional figures and tables as described in the text (PDF)

Crystallographic data for $Pt_2(HMPC)_4$ (CIF)

https://doi.org/10.1021/jacsau.1c00388
JACS Au 2022, 2, 109−115

Crystallographic data for **1** (CIF)

Crystallographic data for **1A** (CIF)

Crystallographic data for **1H** (CIF)

Accession Codes

CCDC 2075516−2075519 contain the supplementary crystallographic data for this paper. These data can be obtained free of charge via www.ccdc.cam.ac.uk/data_request/cif, or by emailing data_request@ccdc.cam.ac.uk, or by contacting The Cambridge Crystallographic Data Centre, 12 Union Road, Cambridge CB2 1EZ, UK; Fax: +44 1223 336033.

AUTHOR INFORMATION

Corresponding Authors

Kazuya Otsubo − *Division of Chemistry, Graduate School of Science, Kyoto University, Kyoto 606-8502, Japan;* orcid.org/0000-0003-4688-2822; Email: kazuya@kuchem.kyoto-u.ac.jp

Hiroshi Kitagawa − *Division of Chemistry, Graduate School of Science, Kyoto University, Kyoto 606-8502, Japan;* orcid.org/0000-0001-6955-3015; Email: kitagawa@kuchem.kyoto-u.ac.jp

Authors

Shuya Nagayama − *Division of Chemistry, Graduate School of Science, Kyoto University, Kyoto 606-8502, Japan*

Shogo Kawaguchi − *Japan Synchrotron Radiation Research Institute (JASRI), SPring-8, Sayo-gun, Hyogo 679-5198, Japan*

Kunihisa Sugimoto − *Japan Synchrotron Radiation Research Institute (JASRI), SPring-8, Sayo-gun, Hyogo 679-5198, Japan;* orcid.org/0000-0002-0103-8153

Complete contact information is available at: https://pubs.acs.org/10.1021/jacsau.1c00388

Author Contributions

K.O. and H.K. conceived the work and designed this study. S.N. contributed to the synthesis, basic characterization, and proton conductivity measurements. Single-crystal X-ray analyses, Rietveld refinements, DFT calculations, and single-crystal proton conductivity measurements were performed by K.O. Synchrotron XRD measurements were supported by K.S. and S.K. K.O. and H.K. cowrote the manuscript. All the authors discussed and commented on the paper.

Notes

The authors declare no competing financial interest.

ACKNOWLEDGMENTS

This work was supported by the Core Research for Evolutional Science and Technology "Creation of Innovative Functions of Intelligent Materials on the Basis of the Element Strategy", ACCEL from the Japan Science and Technology Agency, a Grant-in-Aid for Specially Promoted Research (20H05623), and JSPS KAKENHI Grants JP20350030, JP23245012, JP15H05479, JP17H05366, JP19K05494, and JP19H04572 (Coordination Asymmetry). Synchrotron X-ray diffraction measurements were supported by the Japan Synchrotron Radiation Research Institute (Proposals 2018A1428, 2019A1132, 2020A1206, and 2021A1296).

REFERENCES

(1) Furukawa, H.; Cordova, K. E.; O'Keeffe, M.; Yaghi, O. M. The Chemistry and Applications of Metal−Organic Frameworks. *Science* **2013**, *341*, 1230444.

(2) Li, J.-R.; Sculley, J.; Zhou, H.-C. Metal−Organic Frameworks for Separations. *Chem. Rev.* **2012**, *112*, 869−932.

(3) Yoon, M.; Srirambalaji, R.; Kim, K. Homochiral Metal−Organic Frameworks for Asymmetric Heterogeneous Catalysis. *Chem. Rev.* **2012**, *112*, 1196−1231.

(4) Murray, L. J.; Dinca, M.; Long, J. R. Hydrogen storage in metal−organic frameworks. *Chem. Soc. Rev.* **2009**, *38*, 1294−1314.

(5) Horike, S.; Shimomura, S.; Kitagawa, S. Soft porous crystals. *Nat. Chem.* **2009**, *1*, 695−704.

(6) Bansal, R. C.; Goyal, M. *Activated Carbon Adsorption*; CRC Press: 2005.

(7) Marsh, H.; Reinoso, F. R. *Activated Carbon*; Elsevier Science: 2006.

(8) Breck, D. W. *Zeolite Molecular Sieves: Structure, Chemistry, and Use*; Wiley: 1974.

(9) Cundy, C. S.; Cox, P. A. The Hydrothermal Synthesis of Zeolites: History and Development from the Earliest Days to the Present Time. *Chem. Rev.* **2003**, *103*, 663−701.

(10) Zhao, D.; Timmons, D. J.; Yuan, D.; Zhou, H.-C. Tuning the Topology and Functionality of Metal−Organic Frameworks by Ligand Design. *Acc. Chem. Res.* **2011**, *44*, 123−133.

(11) Brozek, C. K.; Dinca, M. Cation exchange at the secondary building units of metal−organic frameworks. *Chem. Soc. Rev.* **2014**, *43*, 5456−5467.

(12) Schoedel, A.; Li, M.; Li, D.; O'Keeffe, M.; Yaghi, O. M. Structures of Metal−Organic Frameworks with Rod Secondary Building Units. *Chem. Rev.* **2016**, *116*, 12466−12535.

(13) Li, X.; Yang, X.; Xue, H.; Pang, H.; Xu, Q. Metal−organic frameworks as a platform for clean energy applications. *Energy Chem.* **2020**, *2*, 100027.

(14) Ariga, K.; Shionoya, M. Nanoarchitectonics for Coordination Asymmetry and Related Chemistry. *Bull. Chem. Soc. Jpn.* **2021**, *94*, 839−859.

(15) Yamada, T.; Otsubo, K.; Makiura, R.; Kitagawa, H. Designer coordination polymers: dimensional crossover architectures and proton conduction. *Chem. Soc. Rev.* **2013**, *42*, 6655−6669.

(16) Ramaswamy, P.; Wong, N. E.; Shimizu, G. K. H. MOFs as proton conductors − challenges and opportunities. *Chem. Soc. Rev.* **2014**, *43*, 5913−5932.

(17) Lim, D.-W.; Kitagawa, H. Proton Transport in Metal−Organic Frameworks. *Chem. Rev.* **2020**, *120*, 8416−8467.

(18) Lee, J.-S. M.; Otake, K.-i.; Kitagawa, S. Transport properties in porous coordination polymers. *Coord. Chem. Rev.* **2020**, *421*, 213447.

(19) Zhang, G.; Jin, L.; Zhang, R.; Bai, Y.; Zhu, R.; Pang, H. Recent advances in the development of electronically and ionically conductive metal-organic frameworks. *Coord. Chem. Rev.* **2021**, *439*, 213915.

(20) Sadakiyo, M.; Yamada, T.; Kitagawa, H. Rational Designs for Highly Proton-Conductive Metal−Organic Frameworks. *J. Am. Chem. Soc.* **2009**, *131*, 9906−9907.

(21) Sadakiyo, M.; Yamada, T.; Kitagawa, H. Hydrated Proton-Conductive Metal−Organic Frameworks. *ChemPlusChem* **2016**, *81*, 691−701.

(22) Agmon, N. The Grotthuss mechanism. *Chem. Phys. Lett.* **1995**, *244*, 456−462.

(23) Kreuer, K.-D.; Paddison, S. J.; Spohr, E.; Schuster, M. Transport in proton conductors for fuel-cell applications: simulations, elementary reactions, and phenomenology. *Chem. Rev.* **2004**, *104*, 4637−4678.

(24) Kreuer, K.-D.; Rabenau, A.; Weppner, W. Vehicle mechanism, a new model for the interpretation of the conductivity of fast proton conductors. *Angew. Chem., Int. Ed. Engl.* **1982**, *21*, 208−209.

(25) Roundhill, D. M.; Gray, H. B.; Che, C. M. Pyrophosphito-bridged diplatinum chemistry. *Acc. Chem. Res.* **1989**, *22*, 55−61.

(26) Mitsumi, M.; Ueda, H.; Furukawa, K.; Ozawa, Y.; Toriumi, K.; Kurmoo, M. Constructing Highly Conducting Metal−Metal Bonded Solids by Electrocrystallization of $[Pt^{II}_2(RCS_2)_4]$ (RCS_2^- = Dithiocarboxylato, R = Methyl or Ethyl). *J. Am. Chem. Soc.* **2008**, *130*, 14102−14104.
(27) Moriyama, H.; Otsubo, K.; Aoki, K.; Maesato, M.; Sugimoto, K.; Kitagawa, H. A Novel Platinum(III)−Platinum(III) Neutral Dimer Complex, $Pt_2(cdtb)_4I_2$ (cdtb: 4-Cyanodithiobenzoate). *Chem. Lett.* **2019**, *48*, 1035−1037.
(28) Kato, M.; Omura, A.; Toshikawa, A.; Kishi, S.; Sugimoto, Y. Vapor-Induced Luminescence Switching in Crystals of the Syn Isomer of a Dinuclear (Bipyridine)platinum(II) Complex Bridged with Pyridine-2-Thiolate Ions. *Angew. Chem., Int. Ed.* **2002**, *41*, 3183−3185.
(29) Saito, D.; Ogawa, T.; Yoshida, M.; Takayama, J.; Hiura, S.; Murayama, A.; Kobayashi, A.; Kato, M. Intense Red-Blue Luminescence Based on Superfine Control of Metal−Metal Interactions for Self-Assembled Platinum(II) Complexes. *Angew. Chem., Int. Ed.* **2020**, *59*, 18723−18730.
(30) Bellitto, C.; Flamini, A.; Gastaldi, L.; Scaramuzza, L. Halogen oxidation of tetrakis(dithioacetato)diplatinum(II) complexes, $Pt_2(CH_3CS_2)_4$. Synthesis and characterization of $Pt_2(CH_3CS_2)_4X_2$ (X = Cl, Br, I) and structural, electrical, and optical properties of linear-chain (μ-iodo)tetrakis(dithioacetato)diplatinum, $Pt_2(CH_3CS_2)_4I$. *Inorg. Chem.* **1983**, *22*, 444−449.
(31) Che, C. M.; Herbstein, F. H.; Schaefer, W. P.; Marsh, R. E.; Gray, H. B. Binuclear platinum diphosphite complexes. Crystal structures of tetrapotassium bromotetrakis(diphosphito)diplatinate trihydrate ($K_4[Pt_2(pop)_4Br]\cdot 3H_2O$), a new linear chain semiconductor, and tetrapotassium dichlorotetrakis(diphosphito)-diplatinate dihydrate ($K_4[Pt_2(pop)_4Cl_2]\cdot 2H_2O$). *J. Am. Chem. Soc.* **1983**, *105*, 4604−4607.
(32) Otsubo, K.; Kobayashi, A.; Kitagawa, H.; Hedo, M.; Uwatoko, Y.; Sagayama, H.; Wakabayashi, Y.; Sawa, H. Most Stable Metallic Phase of the Mixed-Valence MMX-Chain, $Pt_2(dtp)_4I$ (dtp = $C_2H_5CS_2^-$), in Purely *d*-Electronic Conductors Based on the Transition-Metal Complex. *J. Am. Chem. Soc.* **2006**, *128*, 8140−8141.
(33) Iguchi, H.; Takaishi, S.; Miyasaka, H.; Yamashita, M.; Matsuzaki, H.; Okamoto, H.; Tanaka, H.; Kuroda, S. Water-Vapor-Induced Reversible Switching of Electronic States in an MMX-Type Chain Complex with Retention of Single Crystallinity. *Angew. Chem., Int. Ed.* **2010**, *49*, 552−555.
(34) Yamashita, M.; Okamoto, H. *Material Designs and New Physical Properties in MX- and MMX-Chain Compounds*; Springer-Verlag: 2013.
(35) Ghasempour, H.; Wang, K. Y.; Powell, J. A.; ZareKarizi, F.; Lv, X.-L.; Morsali, A.; Zhou, H.-C. Metal−organic frameworks based on multicarboxylate linkers. *Coord. Chem. Rev.* **2021**, *426*, 213542.
(36) Bao, S.-S.; Li, N.-Z.; Taylor, J. M.; Shen, Y.; Kitagawa, H.; Zheng, L.-M. Co−Ca Phosphonate Showing Humidity-Sensitive Single Crystal to Single Crystal Structural Transformation and Tunable Proton Conduction Properties. *Chem. Mater.* **2015**, *27*, 8116−8125.
(37) Joarder, B.; Lin, J.-B.; Romero, Z.; Shimizu, G. K. H. Single Crystal Proton Conduction Study of a Metal Organic Framework of Modest Water Stability. *J. Am. Chem. Soc.* **2017**, *139*, 7176−7179.
(38) Umakoshi, K.; Kinoshita, I.; Ichimura, A.; Ooi, S. Binuclear Platinum(II) and -(III) Complexes of Pyridine-2-thiol and Its 4-Methyl Analogue. Synthesis, Structure, and Electrochemistry. *Inorg. Chem.* **1987**, *26*, 3551−3556.
(39) Spek, A. L. Single-crystal structure validation with the program PLATON. *J. Appl. Crystallogr.* **2003**, *36*, 7−11.
(40) Nagarkar, S. S.; Unni, S. M.; Sharma, A.; Kurungot, S.; Ghosh, S. K. Two-in-One: Inherent Anhydrous and Water-Assisted High Proton Conduction in a 3D Metal−Organic Framework. *Angew. Chem., Int. Ed.* **2014**, *53*, 2638−2642.
(41) Nguyen, N. T. T.; Furukawa, H.; Gándara, F.; Trickett, C. A.; Jeong, H. M.; Cordova, K. E.; Yaghi, O. M. Three-Dimensional Metal−Catecholate Frameworks and Their Ultrahigh Proton Conductivity. *J. Am. Chem. Soc.* **2015**, *137*, 15394−15397.
(42) Tu, T. N.; Phan, N. Q.; Vu, T. T.; Nguyen, H. L.; Cordova, K. E.; Furukawa, H. High proton conductivity at low relative humidity in an anionic Fe-based metal−organic framework. *J. Mater. Chem. A* **2016**, *4*, 3638−3641.
(43) Wei, Y.-S.; Hu, X.-P.; Han, Z.; Dong, X.-Y.; Zang, S.-Q.; Mak, T. C. W. Unique Proton Dynamics in an Efficient MOF-Based Proton Conductor. *J. Am. Chem. Soc.* **2017**, *139*, 3505−3512.
(44) Otake, K.-i.; Otsubo, K.; Komatsu, T.; Dekura, S.; Taylor, J. M.; Ikeda, R.; Sugimoto, K.; Fujiwara, A.; Chou, C.-P.; Sakti, A. W.; Nishimura, Y.; Nakai, H.; Kitagawa, H. Confined water-mediated high proton conduction in hydrophobic channel of a synthetic nanotube. *Nat. Commun.* **2020**, *11*, 843.
(45) Gerhardt, R. Impedance and dielectric spectroscopy revisited: Distinguishing localized relaxation from long-range conductivity. *J. Phys. Chem. Solids* **1994**, *55*, 1491−1506.
(46) Yamamura, S.; Takata, M.; Sakata, M.; Sugawara, Y. Nature of the Hydrogen Bond in Tetragonal KDP (KH_2PO_4) Observed by Maximum Entropy Method. *J. Phys. Soc. Jpn.* **1998**, *67*, 4124−4127.

https://doi.org/10.1021/jacsau.1c00388
JACS Au 2022, 2, 109−115